CrossMark

Can Emission Measure Distributions Derived from Extreme-ultraviolet Images Accurately Constrain High-temperature Plasma?

P. S. Athiray[1,2] and Amy R. Winebarger[2]
[1] Center for Space Plasma and Aeronomic Research, The University of Alabama in Huntsville, Huntsville, AL 35899, USA; athiray.panchap@nasa.gov
[2] NASA Marshall Space Flight Center, ST13, Huntsville, AL 35812, USA

Abstract

Measuring the relative amount of high-temperature, low emission measure (EM) plasma is considered to be a smoking-gun observation to constrain the frequency of plasma heating in coronal structures. Often, narrowband, extreme-ultraviolet images, such as those obtained by the Atmospheric Imaging Assembly (AIA) on the Solar Dynamics Observatory (SDO), are used to determine the EM distribution, though the sensitivity to high-temperature plasma is limited. Conversely, the soft X-ray wavelength range offers multiple high-temperature diagnostics, including emission lines of N VII, O VII, O VIII, Fe XVII, Ne IX, and Mg XI, which can provide tight constraints to the high-temperature plasma in the $\log T = 6.1$–6.7 ($\sim$1–5+ MK) range. The Marshall Grazing Incidence X-ray Spectrometer (MaGIXS), a slitless spectrograph launched on a NASA sounding rocket on 2021 July 30, resolved an X-ray-bright point in multiple emission lines in the soft X-ray wavelength range. Using coordinated observations of the same X-ray-bright point from SDO/AIA, we compare and contrast the EM distributions from the EUV image data, the X-ray spectra, and the combined EUV and X-ray data set. In this paper, we demonstrate that EM distributions from SDO/AIA data alone can overestimate the amount of high-temperature ($\log T > 6.4$) plasma in the solar corona by a factor of 3–15. Furthermore, we present our effort to cross-calibrate Hinode/X-ray Telescope (XRT) response functions by comparing the observed XRT fluxes with the predicted ones from combined MaGIXS-1 + AIA EM analysis.

Unified Astronomy Thesaurus concepts: Solar coronal heating (1989); Solar corona (1483); Solar extreme ultraviolet emission (1493); Solar x-ray emission (1536); Solar active regions (1974)

1. Introduction

The emission measure (EM) distribution is a useful diagnostic to constrain the frequency of heating events in solar coronal structures including X-ray-bright points and active regions (ARs). The EM distribution represents the amount of thermal plasma integrated along the line of sight derived as a function of temperature. Typical EMs of nonflaring coronal structures exhibit a broken power-law relationship, with hotward (β) and coolward (α) slopes. The slopes can be used as a diagnostic for the heating frequency (Tripathi et al. 2011; Warren et al. 2011; Winebarger et al. 2011; Reep et al. 2013; Athiray et al. 2019).

The continuous, full-Sun, high spatial resolution ($\sim$1″2), narrowband extreme-ultraviolet (EUV) images from the Atmospheric Imaging Assembly (AIA; Lemen et al. 2012) on board Solar Dynamics Observatory (SDO) are commonly used to determine the EM distributions. Six AIA EUV channels are dominated by several iron emission lines of varying ionization states, i.e., 94 Å (Fe XVIII, Fe X), 131 Å (Fe VIII, Fe XX, Fe XXIII), 171 Å (Fe IX), 193 Å (Fe XI, Fe XII, Fe XXIV), and 211 Å (Fe XIV), 335 Å (Fe XVI), but have contributions from several other emissions lines (see O'Dwyer et al. 2010). The three channels sensitive to the highest temperatures (94, 131, and 193 Å) exhibit a bimodal thermal response, which makes it difficult to delineate the relative contribution from hot components from the contributions of cool structures along the same line of sight. Additionally, the high-temperature responses of the 131 and 193 Å channels are from spectral lines only expected during solar flares, leaving a single channel (94 Å) to constrain the high-temperature slopes of typical quiescent coronal structures.

Due to this limitation, the EM distributions derived from AIA images cannot be expected to constrain the emission at high temperatures >5 MK (Su et al. 2018). Attempts have been made to determine a more accurate EM distribution by combining other instruments with AIA. Inclusion of broadband X-ray images from the X-ray Telescope (XRT; Golub et al. 2007) and spectrally superior EUV data from the EUV Imaging Spectrometer (EIS; Culhane et al. 1991), both on the Hinode spacecraft, are often used in conjunction with AIA data to provide additional constraints to the EM solver in narrowing down the T–EM space. However, Winebarger et al. (2012) established that EIS and XRT also exhibit a "blind spot" for high-temperature, low-EM plasma, which indicates that even a combined data set may be insensitive to the hotward EM slope, β. Using synthetic EM distributions with a range of α and β, Athiray et al. (2019) showed that existing space instrumentation cannot precisely determine the slope of the high-temperature emission, and therefore we need instruments with superior spectroscopic capabilities to provide excellent temperature diagnostics, which are accessible in spectral observations in X-rays.

The Marshall Grazing incidence X-ray Spectrometer (MaGIXS) instrument (Athiray et al. 2019; Champey et al. 2022; Savage et al. 2023) was designed to quantitatively measure the high-temperature EM slope by distinctly observing high-temperature diagnostic emission lines. During the first
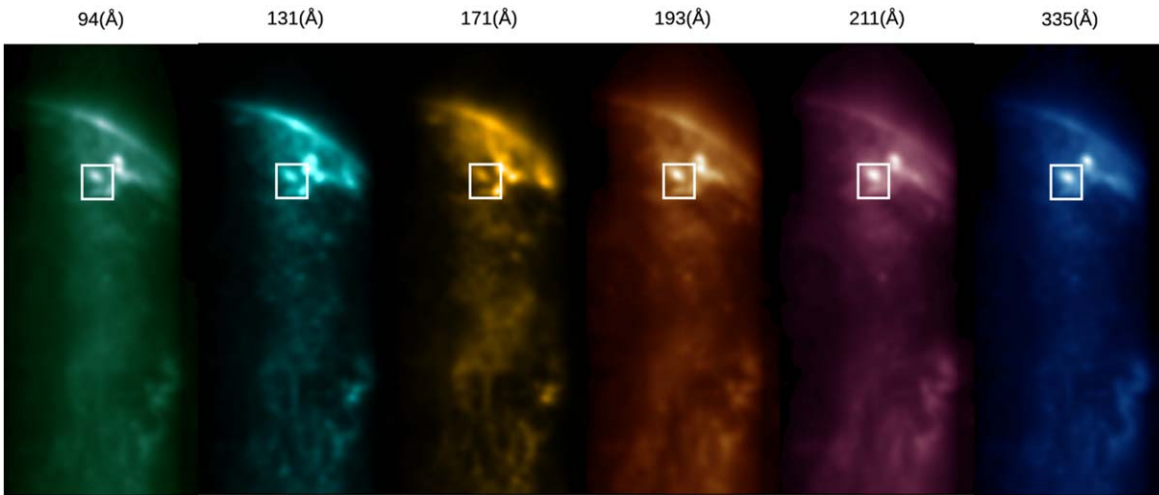
Figure 1. FOV of MaGIXS-1 as seen by AIA, where the AIA resolution has been degraded to match MaGIXS-1. The X-ray-bright point used as an example in this study is highlighted with a box.

sounding rocket flight, MaGIXS-1, the instrument observed spectrally dispersed soft X-ray images of solar coronal structures, from 8 to 30 Å, which has given an excellent opportunity to compare the EM determined using AIA with those derived from X-ray observations. For this comparison, we considered the observation of an X-ray-bright point from MaGIXS-1 as a case study.

In this work, for the first time, we quantify the degree to which EM distributions derived from AIA alone can over-estimate high-temperature, low-EM plasma and demonstrate how a combined AIA and MaGIXS-1 data set can well constrain the complete temperature range expected in quiescent coronal structures. Section 2 describes the data sets and instruments. Section 3 discusses the EM analysis of the X-ray-bright point using MaGIXS-1 and AIA data independently and also presents the first combined EM inversion of MaGIXS-1 spectroheliogram data with AIA images. In Section 4, we compare the predicted fluxes from different EM solutions and quantify the overestimation of high-temperature fluxes using only AIA images. In Section 5, we describe the efforts to cross-calibrate Hinode/XRT with AIA and MaGIXS-1 using the inverted EM solutions. Finally, a summary and conclusions are provided in Section 6.

2. Data and Data Processing

In this section we give a brief summary of the observations from each instrument and describe the process of data preparation for the analysis. The MaGIXS-1 sounding rocket flight occurred on 2021 July 30 from 18:21 to 18:26 UT. The effective MaGIXS-1 field of view (FOV) covers $\sim 9'.25 \times 25'$ on the solar disk (see Figure 1). Due to its limited observation time and FOV, MaGIXS-1 observations define the observational target. The MaGIXS-1 FOV included two X-ray-bright points and a portion of an AR. In this study, we consider one of the X-ray-bright points that was approximately $(625'', 463'')$ from Sun center and to the east of NOAA Active Region 12846, highlighted in Figure 1 with a white box.

The MaGIXS-1 instrument is a wide-field slot imaging X-ray spectrometer, with a direct focusing Wolter-1 X-ray telescope, two corrective grazing incidence X-ray mirrors, and a reflective grating, which disperses X-rays onto the CCD (Champey et al. 2022). MaGIXS-1 observed dispersed X-rays in the

wavelength range ~ 8–30 Å with 2 s cadence for 296 s, during the stable pointing for science observations. MaGIXS-1 data are spectroheliograms, which contain overlapping dispersed spectra arising from different spatial locations on the Sun. The spatial plate scale of MaGIXS-1 is $2''.8$ in the cross-dispersion direction and varies from $\sim 5''.5$ to $9''$ in the dispersion direction. The point-spread function (PSF) of MaGIXS-1 is $\sim 27''$ (Champey et al. 2022). For this analysis, we utilized MaGIXS-1 Level 1.5 data products (see Savage et al. 2023 for a description of the data processing). We average the data over the stable pointing period of science observations of the rocket flight. The MaGIXS-1 observations are modulated by the instrument vignetting function described in Savage et al. (2023). The vignetting function peaks at the center FOV and gradually decreases on both sides of the field, altering the apparent brightness of the observed features. As described in the MaGIXS-1 mission paper, the MaGIXS-1 data have been co-aligned with AIA images using a cross-correlation method to determine the absolute pointing.

SDO/AIA was operational during the MaGIXS-1 flight, observing the full Sun with all EUV passbands. The data have $\sim 1''.2$ spatial resolution ($0''.6$ plate scale) and 12 s temporal cadence. In this analysis, we average the AIA EUV images taken from 18:21 UT to 18:28 UT on 2021 July 30 to match the MaGIXS rocket flight observation. We obtained the cutouts of the full-disk images via the Stanford Joint Science Operations Center (JSOC) Science Data Processing (SDP) center. We selected the MaGIXS-1 FOV with appropriate $23°$ roll angle to match MaGIXS-1 observations. We follow standard AIA routines to co-align data cubes onto a common plate scale via *aia_prep.pro* distributed in the Solar Software (SSW). We rebinned the AIA pixels to a $2''.8$ pixel^{-1} plate scale, while preserving the average intensity per pixel, so as to use the standard AIA temperature response functions. We also multiplied the EUV images by the MaGIXS vignetting function, and finally, the AIA data are convolved with the MaGIXS-1 PSF. Figure 1 shows the time-averaged cutout images of the AIA channels in the MaGIXS-1 FOV with the vignetting function and PSF applied. The X-ray-bright point that is used as an example in this paper is highlighted with a rectangular box.
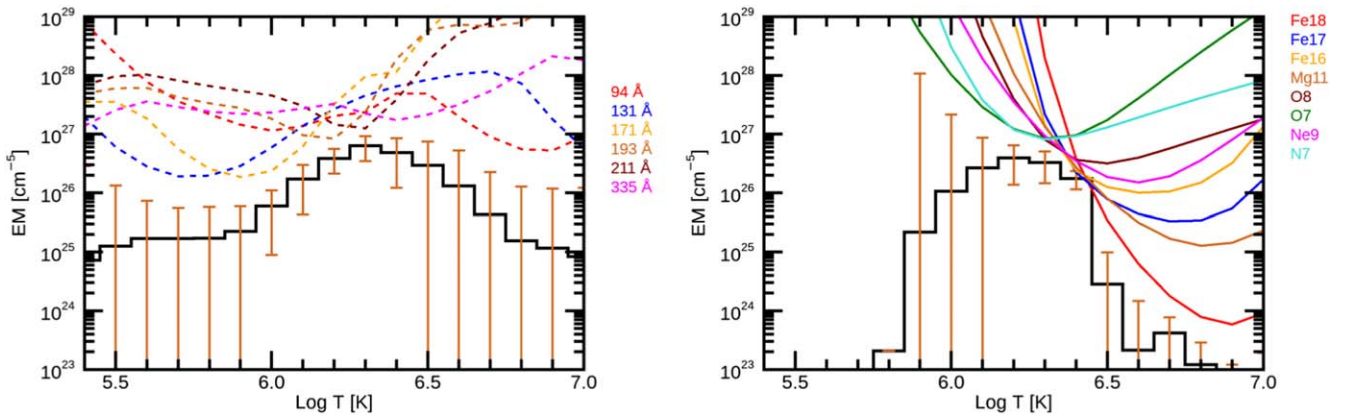
Athiray & Winebarger

Figure 2. The EM solutions obtained for the X-ray-bright point using AIA data (left) and MaGIXS-1 data (right). The best solution for the observed fluxes is shown as a solid black line. The error bars represent change of EM at each temperature bin, while the intensities in either the AIA channel or MaGIXS-1 line are not changed by more than 20% of the best EM solution (see text for additional details). The EM loci curves of the respective channels or spectral lines are overplotted in different colors.

3. Emission Measure Analysis

The goal of this research is to quantify the differences in the EM distributions derived from using AIA data alone, MaGIXS-1 data alone, and a combined MaGIXS-1 and AIA data set. To complete this goal, we use the X-ray-bright point observed by both MaGIXS-1 and AIA. We use six AIA passband data, namely 94 Å, 131 Å, 171 Å, 193 Å, 211 Å, and 335 Å (see Figure 1), for the EM analysis. Further, we note that no signature of bursty impulsive heating events such as brightening and/or microflares is observed from this bright point, and the emission is very steady during this time of observation, consistent with high-frequency heating (Savage et al. 2023).

3.1. SDO/AIA Alone

To determine the EM distribution of the observed plasma using AIA data alone, we first find the EM distribution in the pixels within the region of interest (rectangular box) in Figure 1. Determination of EM from a set of spectrally impure narrowband AIA observations is an underdetermined problem. For this analysis we use the "standard" EM solver distributed by the AIA team, *aia_sparse_em_init.pro*, in the AIA software with its standard settings (Cheung et al. 2015), predict high-temperature diagnostic MaGIXS-1 line intensities, and compare with measurements to determine the extent of under/overestimation.

The standard AIA EM technique relies on the assumption that the EM distribution is a linear sum of a series of basis functions, which are Gaussian functions in log T with varying widths. The routine then finds a sparse EM solution such that the basis function multiplied by the coefficients and convolved with the temperature response functions minimizes the difference in the observed and modeled intensities. Because the EM distribution is assumed to be a sum of Gaussian functions and the inversion algorithm favors sparse solution, the EM distribution is optimized for both sparse and smooth solutions.

The temperature response functions for the SDO/AIA channels are generated using *aia_get_response.pro* with flags timedepend_date, eve_norm, and chianti-fix, using CHIANTI database version 10.1 (Dere et al. 2023). The errors on the AIA intensities are estimated from the function *aia_bp_estimate_error.pro* provided by the SDO package in the SSW, which takes

a number of instrumental effects into account. The generated response functions have coronal abundances (Feldman et al. 1992), ionization equilibrium, and assumed Maxwellian thermal electron distribution. The inversion is carried out using default basis widths (σ) of 0.1, 0.2, and 0.6 in log T.

The resulting EM distribution and the corresponding AIA EM loci curves are shown in the left panel of Figure 2. The EM distribution peaks at log $T = 6.3$ and falls off gradually toward higher temperatures. Note that the EM loci curves indicate that the AIA 94 Å channel is the only constraint of the EM distribution at high temperatures (log $T > 6.6$).

We assess the fidelity of the best EM solution by adopting a similar approach from Winebarger et al. (2012). We calculate how much EM can be added or removed in each temperature bin without varying the intensities in any AIA channel by more than 20%, typical calibration uncertainty for AIA filter response functions (Guennou et al. 2013), and larger than the statistical uncertainty in the average values.

The result is shown as error bars on the EM curve in the left panel of Figure 2. These error bars show that the EM curve is well constrained in the temperature range $6.0 \leqslant \log T \leqslant 6.4$, meaning that small changes in the EM in those bins result in a change in the AIA intensity in at least one channel that would be larger than the uncertainty in the calibration. The EM is poorly constrained outside this range, indicating that the solution can vary significantly and have little impact on the intensities. We mention that the error bars shown here do not represent statistical error and/or other systematic uncertainties. Instead, they signify the collective sensitivity of AIA channels to individual temperature bins at which an appreciable change in the AIA intensities can be observed.

3.2. MaGIXS-1 Alone

Next, we calculate the EM distribution using only MaGIXS-1 data with the method described in Savage et al. (2023) and following the general procedures described in Cheung et al. (2019) and Winebarger et al. (2019). We first cast the problem as a set of linear equations, namely

$$y = Mx, \tag{1}$$

where *y* is a one-dimensional array that contains a single row of the MaGIXS-1 flight data, *x* is a one-dimensional array of EMs
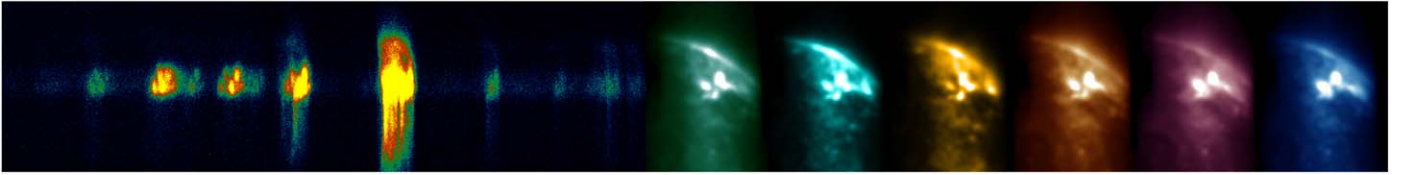
Figure 3. Combined MaGIXS-1 and AIA coordinated data used for joint EM analysis.

at different solar locations and temperatures, and M is a matrix that maps emission from each solar location and temperature into the detector. The MaGIXS-1 response matrix, M, is generated using the wavelength calibration as a function of field angle determined from flight data and effective area measured preflight (Athiray et al. 2021). Using the CHIANTI atomic database version 10.1 (Dere et al. 2023; with additional Fe XVI lines—see updates below), we construct isothermal, unit EM instrument response functions with coronal abundances, Maxwellian electron distribution, and an assumption of ionization equilibrium. These assumptions were based on the best-fit solutions given in Savage et al. (2023).

Solving Equation (1) for spectroheliograms is challenging, as y contains a large number of features, which are highly correlated. We use the ElasticNet regularization technique (Zou & Hastie 2005), a commonly used approach in machine learning to solve linear regression problems, available in Scikit learn via the Python library. It combines two types of regularization, namely the sparsity and smoothness, while finding convergence to the best solution, which is defined by

$$x^{\#} = \mathrm{argmin}[||W(y - Mx)||_2^2 + \alpha\rho||x||_1$$
$$+ 0.5\alpha(1 - \rho)||x||_2^2], \qquad (2)$$

where α and ρ are hyperparameters. α is the magnitude of the penalty term, and ρ is varied from 0 to 1 to adjust whether the solution is smoother ($\rho \to 0$) or sparser ($\rho \to 1$). The first term in Equation (2) is the standard weighted least-squares term that minimizes the difference between the observations and the forward-calculated observations. The weights, W, are a diagonal matrix where the values are $1/\sigma$ and σ is the quadrature sum of read and photon noise. The second term in Equation (2) is the L_1 norm of x; minimizing this term favors a sparse solution. The third term is the L_2 norm of x; minimizing this term favors a smooth solution. Another free parameter is the spatial resolution of the inverted solution, $\delta\theta$. We have carried out a systematic study of α, ρ, and $\delta\theta$ and find that a wide range of parameters yield near-identical solutions. Results and inferences from the systematic study are beyond the scope of this work and will be reported elsewhere (P. S. Athiray et al. 2023, in preparation). The solutions shown here use $\alpha = 5 \times 10^{-5}$, $\rho = 0.1$, and $\delta\theta = 8''.4$. As mentioned above, the spatial plate scale of MaGIXS-1 in the dispersion direction varies as a function of wavelength from $\sim5''.5$ to $9''$ pixel^{-1}, while the spatial resolution is $\sim27''$ (see Champey et al. 2022). We find that the resolution of the inversion, $\delta\theta$, being roughly a factor of 3 smaller than the PSF is optimal (P. S. Athiray et al. 2023, in preparation).

We highlight the two updates to the inversion of MaGIXS-1 spectroheliogram data compared to the description given in Savage et al. (2023). The first update is for the response

function, M, which incorporates some new atomic calculations pertaining to the transitions of Fe XVI. Savage et al. (2023) reported an excess emission in MaGIXS-1 observation compared to the inversion near 15 Å and hypothesized that it was due to the missing atomic transitions corresponding to satellite emission lines in that wavelength range. Based on a MaGIXS-1 team request, additional transitions for Fe XVI have been provided to the team to complete this updated inversion and will be added to the CHIANTI database at its next release (Giulio Del Zanna, private communication). In this paper, we include the updated Fe XVI transitions in the MaGIXS-1 response functions. This inclusion significantly improved the spectral fits to the flight data. A paper summarizing the results of new line identification from MaGIXS-1 is under preparation. The second update is the addition of weights to the inversion method (see Equation (2)), which was not employed in the mission paper. The addition of weights improves the inversion and removes minor artifacts arising as a result of spatio-spectral confusion (see Athiray et al. for additional details).

We average the returned EM distribution over the bright point in question. We show the average EM distribution along with the EM loci plots for the key MaGIXS-1 spectral lines in the right panel of Figure 2. Compared to the EM distribution calculated using AIA alone (left), the amount of high-temperature plasma is significantly less and much more constrained by the MaGIXS-1 spectral lines. However, because MaGIXS-1 has no low-temperature sensitivity, the shape of the EM distribution is dominated by the smooth/sparse requirements of the solution, and not by observations, for log $T < 6.1$.

Similar to AIA EM analysis, we vary the EM in every temperature bin and determine how much EM can be added or removed without varying the spectrally pure intensities by more than 20%, the stated calibration uncertainty of MaGIXS-1 (Athiray et al. 2020, 2021). We show this variation in EM as error bars in Figure 2 (right). The EM is well constrained at log $T \geqslant 6.2$. Note that error bars are omitted at temperatures less than log $T = 5.8$ because there are no constraints at these temperatures, meaning that the error bars span the range of EM shown in the plot.

3.3. MaGIXS-1 and AIA

Finally, we combine the MaGIXS-1 spectroheliogram data with narrowband EUV images from AIA to perform a joint EM inversion for the first time. Figure 3 shows the combined MaGIXS-1 and AIA data prepared for a joint EM inversion.

The average EM of the X-ray-bright point determined using MaGIXS-1 and AIA data is shown in Figure 4. When combined, MaGIXS-1 data require a much steeper fall-off of the EM distribution at temperatures log $T \geqslant 6.4$ compared to the AIA-alone inversion. Similarly, the amount of low-temperature EM increases from both the AIA-alone and MaGIXS-1 + AIA solutions. Because MaGIXS-1 is strictly limiting the amount of high-temperature plasma, the EM at low
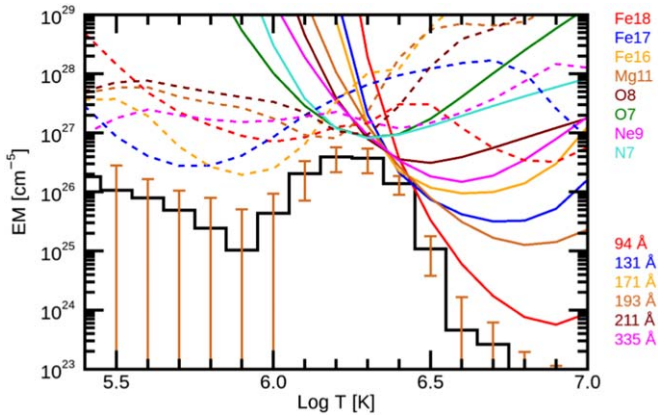
Figure 4. The EM distribution derived using a combined MaGIXS-1 and AIA data set. The best solution that matches the observed fluxes in MaGIXS-1 and AIA is shown as a solid black line; error bars are determined in the same way as AIA and MaGIXS-1 analysis (see text). Overplotted are the EM loci curves of MaGIXS-1 lines (solid colors) and AIA channels (dashed colors).

temperatures has to increase to account for the intensities in the bimodal channels, while in the AIA-alone EM solution some of the intensities in the bimodal channels are accounted for with high-temperature EM. Like the previous calculations, we vary the EM in every temperature bin independently to observe a 20% intensity change in any of the channels/lines used to determine the error bars shown in Figure 4.

4. Quantifying the Overestimation of High-temperature Intensities

In this section, we calculate the average spectral intensities of MaGIXS-1 lines for the spatially averaged X-ray-bright point using the inverted EM solutions. We compare the predicted fluxes determined from inverting only AIA data, only MaGIXS-1 data, and combined MaGIXS-1 and AIA data. The predicted fluxes are determined by folding the respective EM distributions through all the spectral line contribution functions obtained using the CHIANTI database.

Table 1 lists the average spectral intensities in units of $\times 10^{10}$ photons s^{-1} sr^{-1} cm^{-2}. The first and second columns give the ion name, its rest wavelength, and the log T where the emissivity function peaks. We group the spectral lines into three different temperature ranges, log $T = 6.3$, $6.5 \leqslant$ log $T \leqslant 6.6$, and log $T = 6.8$. The third, fourth, and fifth columns give the spectral line fluxes calculated from the EM solutions determined from AIA data only, MaGIXS-1 data only, and combined MaGIXS-1 + AIA data. Here we consider the MaGIXS-1 + AIA EM solution to be the best representation of the plasma temperature distribution. Finally, we then find the intensity ratios for AIA and MaGIXS-1 to the MaGIXS-1 + AIA solution, which are listed in the sixth and seventh columns. A ratio value departing from unity, and above 20%, is considered to overpredict or underpredict the intensities with respect to the intensities determined from the combined EM solution.

The ratio of the intensities calculated from AIA data alone to the MaGIXS-1 + AIA solution (sixth column) clearly shows a systematic overestimation of warm and hot emission lines. We observe a gradual increase in the extent of overestimation for an increase in peak emissivity temperature. For instance, emission lines with peak emissivity temperature log $T = 6.30$ (N VII, O VII) are overestimated by a factor ∼2,

emission lines with peak emissivity temperature of $6.50 \leqslant$ log $T \leqslant 6.60$ (O VIII, Ne IX, and Fe XVI) are overestimated by a factor ∼3–7, and emission lines with peak emissivity temperature at log $T = 6.80$ (Mg XI, Fe XVII) are overestimated by a factor ∼11–15. However, the ratio of MaGIXS-1-alone data to MaGIXS-1 + AIA data did not show a significant change in the predicted fluxes. This result demonstrates that AIA channels do not offer tight constraints to the plasma emission greater than log $T = 6.3$, at which spectral lines from MaGIXS-1 are chosen to precisely determine the low-EM plasma.

5. Cross-calibration with Hinode/XRT

Here we investigate the compatibility of the derived EM solutions with the Hinode/XRT observations by computing the predicted XRT intensities and comparing them with the measured ones. However, during the MaGIXS-1 flight observation, XRT was targeted to observe NOAA AR 12849 near the southwest portion on the disk; hence, there is no coordinated observation available for the bright point under study. Therefore, we consider the nearest time available data from the XRT synoptic data archive, which was ∼30 minutes prior to the MaGIXS-1 observation time, with an assumption that the bright point did not evolve significantly within this duration. We include the Thin-Be/Open, Al-Mesh/Open, and Al-Poly/Open filter combinations with exposure times 23.14, 2.90, and 4.09 s, respectively, in this study. We follow standard XRT data processing methods and determine the average intensity of the X-ray-bright point, which is given in Table 2 (second column).

Our aim here is to predict the average XRT intensity for the bright point using different EM solutions and compare it with the measured intensity from the three filter combinations. Particularly, the joint EM solution with MaGIXS-1 and AIA gives an excellent opportunity to cross-calibrate the XRT response, which has a good overlap in the temperature sensitivity. We calculate the predicted intensities for different EM solutions by folding EM through the standard XRT filter temperature response functions obtained using solar soft routine *make_xrt_temp_resp.pro* using appropriate time-dependent contamination, which are given in Table 3 (third, fourth, and fifth columns). We observe that AIA EM solution systematically overpredicts XRT intensity by a factor of 1.4–4, whereas MaGIXS-1 and MaGIXS-1 + AIA solutions systematically underpredict XRT intensity. Interestingly, the predicted intensities for all three XRT filters using MaGIXS-1 alone and MaGIXS-1 + AIA EM solutions are consistently smaller by a factor ∼2.0. We interpret the excess emission predicted by the AIA-alone solution as due to the fact that AIA channel response functions are insensitive to high-temperature emission, log $T \geqslant 6.5$ (see Athiray et al. 2019), where XRT is sensitive. MaGIXS-1 data include spectral lines that offer precise high-temperature diagnostics. Therefore, predictions of XRT intensities from MaGIXS-1 alone and MaGIXS-1 + AIA EM would offer unique insights into cross-calibration of the instruments. The predicted XRT intensities yield values a factor ∼2 lower than the measured XRT intensities, which would indicate that XRT temperature response functions require a cross-calibration factor (∼2).

Table 1
Average Line Intensities in Some of the Key MaGIXS-1 Spectral Lines Predicted Using Different EM Solutions

Spectral Line (Å)	Temperature (log T)	Predicted Intensity Using EM Solutions $\times 10^{10}$ photons s^{-1} sr^{-1} cm^{-2}			Ratios	
		AIA	MaGIXS-1	MaGIXS-1 + AIA	AIA/ MaGIXS-1 + AIA	MaGIXS-1/ MaGIXS-1 + AIA
N VII 24.770	6.30	4.10	2.05	2.07	1.98	0.99
O VII 21.602	6.30	34.40	18.49	18.42	1.87	1.00
O VII 21.801	6.30	6.28	3.63	3.61	1.74	1.01
O VII 22.101	6.30	25.46	14.65	14.54	1.75	1.01
O VII 18.627	6.30	4.22	2.11	2.11	2.00	1.00
O VIII 18.967	6.50	19.62	5.47	5.36	3.66	1.02
O VIII 16.006	6.50	2.08	0.53	0.51	4.08	1.04
Ne IX 13.447	6.60	2.36	0.48	0.47	5.02	1.02
Ne IX 13.553	6.60	0.49	0.11	0.11	4.45	1.00
Ne IX 13.699	6.60	1.68	0.38	0.38	4.42	1.00
Fe XVI 15.211	6.60	1.73	0.26	0.24	7.21	1.08
Mg XI 9.169	6.80	0.62	0.04	0.04	15.5	1.00
Fe XVII 15.013	6.80	13.53	1.02	0.98	13.81	1.04
Fe XVII 15.262	6.80	4.01	0.31	0.30	13.37	1.03
Fe XVII 15.453	6.80	0.90	0.08	0.08	11.25	1.00
Fe XVII 16.776	6.80	10.64	0.95	0.90	11.82	1.06
Fe XVII 17.051	6.80	14.25	1.29	1.22	11.68	1.06

Table 2
Comparison of the Measured XRT Intensities for the X-Ray-bright Point with the Values Predicted Using Different EM Solutions

Hinode/XRT Channel	Measured Intensity (DN s^{-1})	Predicted Intensity Using EM Solutions (DN s^{-1})		
		AIA Alone	MaGIXS-1 Alone	MaGIXS-1 + AIA
XRT—Be thin	4.7	18.8	2.1	2.0
XRT—Al Mesh	88.9	126.0	39.0	37.8
XRT—Al Poly	58.6	110.0	24.6	24.0

Table 3
Comparison of the Measured Average Intensities in Six AIA Channels for the X-Ray-bright Point with the Values Predicted Using Different EM Solutions in Units of DN s^{-1}

Channel	Measured Flux (DN s^{-1})	Predicted Flux Using EM Solutions (DN s^{-1})		
		AIA Alone	MaGIXS-1 Alone	MaGIXS-1 + AIA
AIA—94 Å	1.3	1.6	1.1	1.0
AIA—131 Å	5.2	3.6	2.5	5.3
AIA—171 Å	160.0	166.0	194.8	173.8
AIA—193 Å	255.8	257.8	247.2	247.4
AIA—211 Å	95.7	88.9	61.4	65.7
AIA—335 Å	1.7	1.8	1.0	1.3

6. Summary and Discussion

We have presented the results of a detailed analysis of the observations of an X-ray-bright point using MaGIXS-1 sounding rocket and SDO/AIA data to diagnose the plasma temperature distribution. In this work, we carried out an independent EM analysis using the observations from both instruments, and we also performed a joint EM analysis, for the first time, by combining MaGIXS-1 spectroheliogram data with narrowband AIA images. This approach of combined EM analysis with MaGIXS-1 and AIA data provides an unprecedented temperature coverage of $5.4 < \log T < 7.0$, with MaGIXS-1 constraining the shape of fall-off at high temperatures, while the cooler channels of AIA offer constraints to the emission at lower temperatures, as shown in Figure 4.

We use the resultant EM distribution from both instruments combined to predict the fluxes of high-temperature diagnostic MaGIXS-1 lines and compare the results with the EM distribution based on MaGIXS-1 and AIA alone. The comparisons are summarized in Table 1, which shows that the EM distribution using AIA data alone overestimates the line fluxes. Furthermore, the extent of overestimation increases with the peak emissivity temperature of the emission lines. Specifically, the AIA-alone EM solution over-predicts $\log T = 6.3$ by a factor of ~ 2, $\log T = 6.4$–6.6 by a factor of ~ 3–7, and $\log T = 6.8$ by a factor of ~ 11–15. In sharp contrast, the flux predicted using combined MaGIXS-1 + AIA EM distribution matches closely (within 20%) with the results from the MaGIXS-1-alone EM distribution, which is consistent with our expectation that high-temperature
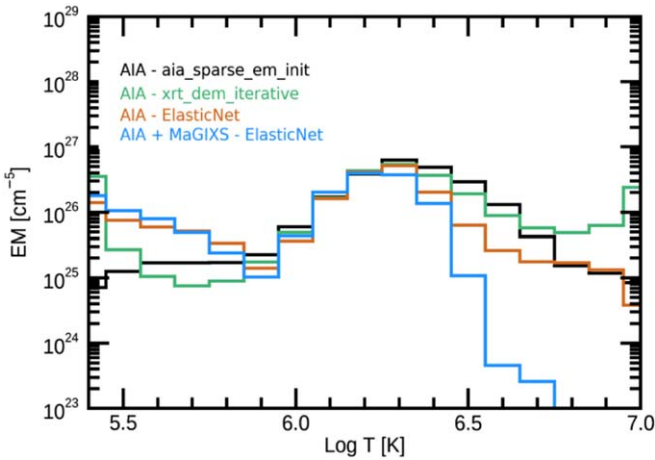
Figure 5. Comparison of EM distribution determined using AIA data only employing different EM solvers, namely *aia_sparse_em_init*, *xrt_dem_iterative*, and ElasticNet, along with the solution using the combined MaGIXS-1 + AIA data set. This clearly demonstrates that the AIA-only solution systematically results in a shallow EM distribution irrespective of the EM solver.

diagnostic lines are accurately modeled using MaGIXS-1 data.

We emphasize that several EM solver algorithms are available to invert AIA EUV data (e.g., Kashyap & Drake 1998; Weber et al. 2004; Aschwanden & Boerner 2011; Hannah & Kontar 2012; Plowman et al. 2013; Cheung et al. 2015), and each method exhibits a set of strengths and also some weaknesses associated with the reconstruction (for instance see Aschwanden et al. 2015; Massa et al. 2023). The output from any solver results in a plausible solution that matches the observed intensities in all six AIA channels. Therefore, different possible solutions are available to any set of AIA observations. Without additional constraints from high-temperature sensitivity instruments like MaGIXS-1, however, we would expect excess high-temperature emission irrespective of the EM solver employed. To validate this, we performed inversion of AIA data only using three different solvers, namely the *aia_sparse_em_init* method (Cheung et al. 2015), the *xrt_dem_iterative* method (Golub et al. 2004; Weber et al. 2004), and the ElasticNet method (Zou & Hastie 2005). The solutions are compared in Figure 5. The first two solvers are the most commonly used and considered as "standard" for EM determination from narrowband images. The ElasticNet method is currently being used for inverting spectroheliogram data such as MaGIXS-1. As expected, different solvers resulted in a different solutions. Qualitatively, Figure 5 shows that inverting AIA data using different solvers systematically overestimates the high-temperature emission, as compared to the solution determined using combined AIA + MaGIXS-1 data. The *aia_sparse_em_init* and *xrt_dem_iterative* method solutions yield similar EM curves at high temperature, while the ElasticNet solution found slightly less EM at log $T = 6.4$–6.7. We hereby infer that the excess high-temperature emission determined by inverting AIA data does not strongly depend on the EM solver method but rather shows the limited sensitivity of AIA channels at these temperatures.

This result is not surprising, as the temperature response of AIA channels does not offer sensitivity to high temperatures alone. Instead, the channels that are sensitive to high temperatures, 94, 131, and 193 Å, exhibit a bimodal response, which means that they can detect both high- and low-

temperature plasma. The low-temperature emission from cool structures along the line of sight often dominates the observed signal, except possibly in flares. Furthermore, the amount of cool plasma along the line of sight limits the sensitivity to high-temperature emission. For instance, consider the EM loci curve of 94 Å (red dashed line) in Figure 2 (left panel). If there were more (less) emission at log $T = 6.1$, the EM loci curve would move higher (lower). The error bars at high temperature would follow this motion, so the uncertainty in the high-temperature emission is directly proportional to the amount of lower-temperature emission along the line of sight. This ambiguity can lead to an overestimation of high-temperature EM. The difficulty in constraining high-temperature, low-EM plasma in AIA channels is akin to the blind spot established in Hinode/ EIS and XRT by Winebarger et al. (2012).

As AIA lacks true high-temperature diagnostics, MaGIXS-1 has no sensitivity to plasma with temperatures less than log $T = 6.1$. Hence, we also use the resultant EM distributions to predict fluxes in the observed AIA channels and then compare them with actual AIA measurements (Table 3). We mention that we only consider calibration uncertainty (20%) on the AIA response functions, based on Guennou et al. (2013), which also lists other possible sources of uncertainties. Therefore, we look for flux variations beyond 20% in the comparison to mark an overestimation or underestimation. We notice that the predicted intensities using the MaGIXS-1-alone solution (third column) underestimate emission in channels 131 Å (~52% less), 211 Å (~36% less), and 335 Å (~42% less). The 131 Å channel exhibits a bimodal response with sensitivity to lower and higher temperatures from Fe VIII, XX, XXIII. Although MaGIXS-1 can detect hot emission from Fe XX, XXIII, which are not observed in the bright point under study, we interpret that 131 Å emission is mainly due to contributions from Fe VIII ~0.5 MK, which MaGIXS-1 cannot detect. Fluxes predicted from MaGIXS-1 + AIA (fourth column) provide a closer agreement for all the AIA channels, which is consistent with the EM loci plots shown in Figure 4.

The slope of the high-temperature EM distribution offers an important constraint on the timescale between heating events (Athiray et al. 2019; Barnes et al. 2019). If the heating occurs at a high frequency, with events spaced at intervals much shorter than a cooling time, the EM distribution will have a steep fall-off at high temperatures, while low-frequency heating will exhibit a shallow hotward slope. The left panel of Figure 6 shows a comparison of the EM solutions from AIA alone, MaGIXS-1 alone, and MaGIXS-1 + AIA data, along with the hotward slope (β) fitted from the peak of the EM distribution. Overestimation of high-temperature emission using AIA data alone gives shallower β compared to the steep β from the MaGIXS-1 and MaGIXS-1 + AIA solutions. This study once again confirms that the X-ray-bright point observed by the MaGIXS-1 flight must be heated at a relatively high frequency so that the loops are close to equilibrium and the distribution of temperatures is narrow.

The combined EM analysis using MaGIXS-1 and AIA instrument data allowed us to investigate the cross-calibration of the Hinode/XRT response functions. Using the XRT synoptic data from the nearest time of MaGIXS-1 observation, we compared the observed XRT intensities in the X-ray-bright point under study against the predicted XRT intensities using the joint EM solution from MaGIXS-1 + AIA. We find that the predicted XRT intensities are smaller, by a factor of ~2, than
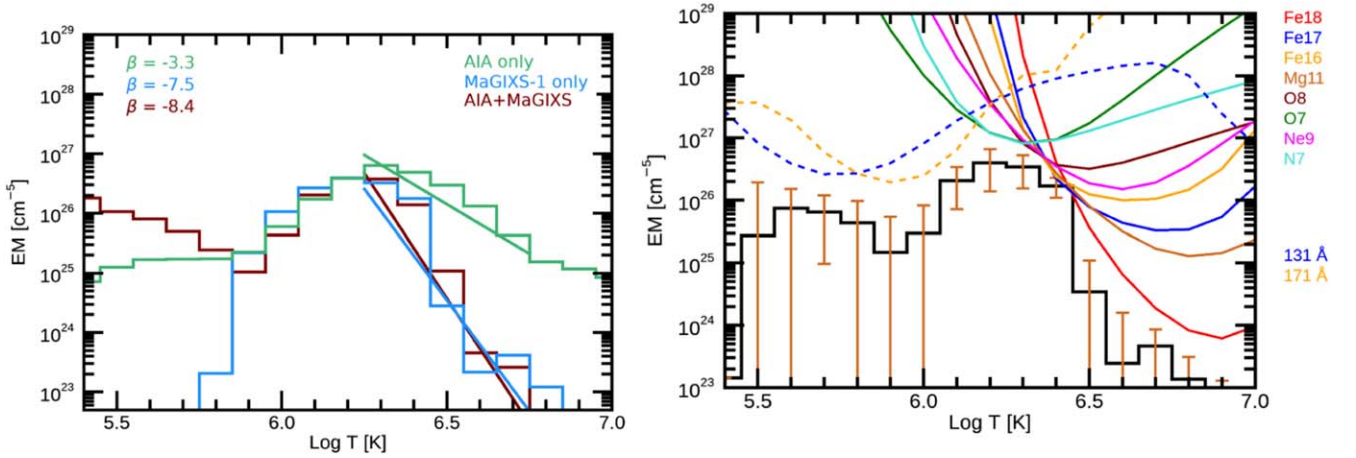
Figure 6. Left: comparison of EM distribution derived using AIA data only, MaGIXS-1 data only, and the combined MaGIXS-1 + AIA data set, along with fits to the high-temperature slope (β). This clearly demonstrates that the AIA-only solution results in a shallow EM distribution compared to the MaGIXS-1-only and MaGIXS-1 + AIA solution, which results in a steep EM distribution. Right: inverted EM solutions with MaGIXS-1 and two AIA channels 131 Å and 171 Å, along with respective EM loci curves (colored curves). This plot portrays that a wide temperature coverage with excellent coronal plasma temperature diagnostics can be achieved with high-resolution X-ray imaging spectroscopy and EUV imagers.

the observed XRT intensities. This implies that XRT response functions require a cross-calibration factor of ~2. This factor agrees closely with several earlier reported studies from combined EM analysis with high-temperature sensitivity X-ray instruments such as NuSTAR and FOXSI (Wright et al. 2017; Athiray et al. 2020). The source for this cross-calibration factor is still unknown. However, we find reports from the earlier years of the Hinode mission comparing the EM distributions from the EUV Imaging Spectrometer (EIS) and XRT, which observe this discrepancy. For instance, Kimble & Schmelz (2011) and Kimble (2011) reported the EIS–XRT cross-calibration factor using X-ray-bright point observations from 2010. The study finds that for a combined EIS–XRT analysis the observed XRT intensities must be multiplied by 0.25, which in other words means multiplying the XRT response functions by a factor of 4. Another study, by Testa et al. (2011), reported EM distributions determined from a coordinated EIS–XRT observation from a nonflaring AR. The study found that EIS EM solutions are consistently smaller than XRT EM solutions by a factor of ~2, while exhibiting similar width and peak temperature. Although the study eluded a cross-calibration factor for a combined EIS–XRT analysis, however, the authors showed and interpreted this discrepancy as due to the influence of elemental abundances (see Testa et al. 2011 for further details). Oddly, no discrepancy between EIS and XRT was found in Winebarger et al. (2012). In addition, investigation by O'Dwyer et al. (2014) showed that observed XRT fluxes agree with EIS observations for ARs and are strongly dependent on the elemental abundances.

We emphasize that MaGIXS-1 is spectrally superior and is a well-calibrated instrument (Athiray et al. 2020, 2021) to precisely quantify the amount of high-temperature plasma, which could be used to cross-calibrate XRT filters owing to a good overlap in the temperature sensitivity. However, lack of coordinated XRT observation for the bright point under study, combined with the uncertainty on the vignetting model, strictly limits our ability to complete the cross-calibration. Nevertheless, this effort strongly motivates the need for cross-calibration of XRT, possibly with the upcoming second flight of MaGIXS-2, scheduled for summer of 2024.

The combined EM analysis using MaGIXS-1 + AIA also revealed an interesting insight into the design of future instrumentation for a wide range of temperature coverage along with high sensitivity. Figure 4 demonstrates that two (131, 171 Å) of the six AIA channels, along with the assumption that the EM curve is smoothly varying, are sufficient to constrain the plasma temperature distribution at temperatures log $T \leqslant 6.1$. To establish this result, we have performed a combined inversion of MaGIXS-1 + AIA with only 131 and 171 Å channels added, which is shown in the right panel of Figure 6. A future instrument design with spatially dispersed spectral images in X-rays combined with 131 and 171 Å EUV images would offer excellent thermal plasma diagnostics covering a wide range of coronal temperatures.

This approach of combined inversion using spatial–spectral overlapped data and images (EUV or X-ray) will set a precedent for the analysis of future missions such as the Cubesat Imaging X-ray Solar Spectrometer (CubIXSS; Caspi et al. 2021) and potential small explorer (currently in Phase A) the EUV CME and Coronal Connectivity Observatory (ECCCO; Reeves et al. 2022), which will carry spectroheliogram instruments along with imagers.

George Mason University, the University of Michigan (USA), the University of Cambridge (UK), and the NASA Goddard Space Flight Center (USA).

ORCID iDs

P. S. Athiray https://orcid.org/0000-0002-4454-147X
Amy R. Winebarger https://orcid.org/0000-0002-5608-531X

References

Aschwanden, M. J., & Boerner, P. 2011, ApJ, 732, 81
Aschwanden, M. J., Boerner, P., Caspi, A., et al. 2015, SoPh, 290, 2733
Athiray, P. S., Winebarger, A. R., Barnes, W. T., et al. 2019, ApJ, 884, 24
Athiray, P. S., Winebarger, A. R., Champey, P., et al. 2020, ApJ, 905, 66
Athiray, P. S., Winebarger, A. R., Champey, P., et al. 2021, ApJ, 922, 65
Barnes, W. T., Bradshaw, S. J., & Viall, N. M. 2019, ApJ, 880, 56
Caspi, A., Shih, A. Y., Panchapakesan, S., et al. 2021, AAS Meeting, 53, 216.09
Champey, P. R., Winebarger, A. R., Kobayashi, K., et al. 2022, JAI, 11, 2250010
Cheung, M. C. M., Boerner, P., Schrijver, C. J., et al. 2015, ApJ, 807, 143
Cheung, M. C. M., De Pontieu, B., Martínez-Sykora, J., et al. 2019, ApJ, 882, 13
Culhane, J. L., Hiei, E., Doschek, G. A., et al. 1991, SoPh, 136, 89
Dere, K. P., Del Zanna, G., Young, P. R., & Landi, E. 2023, ApJS, 268, 52
Feldman, U., Mandelbaum, P., Seely, J. F., Doschek, G. A., & Gursky, H. 1992, ApJS, 81, 387
Golub, L., Deluca, E., Austin, G., et al. 2007, SoPh, 243, 63
Golub, L., Deluca, E. E., Sette, A., & Weber, M. 2004, in ASP Conf. Ser. 325, The Solar-B Mission and the Forefront of Solar Physics, ed. T. Sakurai & T. Sekii (San Francisco, CA: ASP), 217

Guennou, C., Auchère, F., Klimchuk, J. A., Bocchialini, K., & Parenti, S. 2013, ApJ, 774, 31
Hannah, I. G., & Kontar, E. P. 2012, A&A, 539, A146
Kashyap, V., & Drake, J. J. 1998, ApJ, 503, 450
Kimble, J. 2011, PhD thesis, Univ. Memphis
Kimble, J., & Schmelz, J. T. 2011, AAS Meeting, 218, 224.21
Lemen, J. R., Title, A. M., Akin, D. J., et al. 2012, SoPh, 275, 17
Massa, P., Emslie, A. G., Hannah, I. G., & Kontar, E. P. 2023, A&A, 672, A120
O'Dwyer, B., Del Zanna, G., & Mason, H. E. 2014, A&A, 561, A20
O'Dwyer, B., Del Zanna, G., Mason, H. E., Weber, M. A., & Tripathi, D. 2010, A&A, 521, A21
Plowman, J., Kankelborg, C., & Martens, P. 2013, ApJ, 771, 2
Reep, J. W., Bradshaw, S. J., & McAteer, R. T. J. 2013, ApJ, 778, 76
Reeves, K., Seaton, D. B., Golub, L., et al. 2022, AGUFM, 2022, SH23A–06
Savage, S. L., Winebarger, A. R., Kobayashi, K., et al. 2023, ApJ, 945, 105
Su, Y., Veronig, A. M., Hannah, I. G., et al. 2018, ApJL, 856, L17
Testa, P., Reale, F., Landi, E., DeLuca, E. E., & Kashyap, V. 2011, ApJ, 728, 30
Tripathi, D., Klimchuk, J. A., & Mason, H. E. 2011, ApJ, 740, 111
Warren, H. P., Ugarte-Urra, I., Young, P. R., & Stenborg, G. 2011, ApJ, 727, 58
Weber, M. A., Deluca, E. E., Golub, L., & Sette, A. L. 2004, in IAU Symp. 223, Multi-Wavelength Investigations of Solar Activity, ed. A. V. Stepanov, E. E. Benevolenskaya, & A. G. Kosovichev (Cambridge: Cambridge Univ. Press), 321
Winebarger, A. R., Schmelz, J. T., Warren, H. P., Saar, S. H., & Kashyap, V. L. 2011, ApJ, 740, 2
Winebarger, A. R., Warren, H. P., Schmelz, J. T., et al. 2012, ApJL, 746, L17
Winebarger, A. R., Weber, M., Bethge, C., et al. 2019, ApJ, 882, 12
Wright, P. J., Hannah, I. G., Grefenstette, B. W., et al. 2017, ApJ, 844, 132
Zou, H., & Hastie, T. 2005, Journal of the Royal Statistical Society, 67, 301